RSC Applied Polymers

ROYAL SOCIETY OF CHEMISTRY

PAPER

View Article Online
View Journal | View Issue

Cite this: *RSC Appl. Polym.*, 2025, **3**, 1011

Vinylene-bridged naphthalenediimide-based dual-acceptor copolymers for thin-film transistors and solar steam generation†

Chia-Yang Lin,‡[a] Guan-Lin Wu,‡[b] Ting-Yu Wang,[b] Waner He,[a] Ying-Sheng Wu,[b] Shunsuke Imaoka,[a] Shohei Shimizu,[a] Wen-Chang Chen,[b,c] Yoshimitsu Sagara,[a] Chu-Chen Chueh *[b] and Tsuyoshi Michinobu *[a]

Recent studies have shown that introducing vinylene bridges into naphthalenediimide (NDI)-based dual-acceptor copolymers is an effective strategy to improve backbone coplanarity and charge transport properties in organic field-effect transistors (OFETs). However, their potential as multifunctional materials for broader optoelectronic applications remains unexplored. In this study, we designed and synthesized four vinylene-bridged NDI (**vNDI**)-based conjugated polymers containing benzothiadiazole (**S**), benzotriazole (**N**), triazolobenzothiadiazole (**NS**), and benzobistriazole (**NN**) as second acceptors. Structural analysis revealed that the backbone conformation and electron-withdrawing ability of the acceptors significantly influence optical and electronic properties. Among them, **vNDI-NS** exhibited the narrowest optical bandgap (1.05 eV), while **vNDI-N** displayed the highest ambipolar mobility in OFETs, attributed to enhanced crystallinity and improved π–π stacking. Furthermore, these polymers were applied as photothermal membranes in solar steam generation (SSG) devices. Films based on **vNDI-NS** and **vNDI-NN** achieved solar-to-vapor conversion efficiencies of 58.3% and 56.4%, respectively, under 1 sun illumination. This study expands the applications of **vNDI**-based polymers beyond OFETs, providing a dual-functional platform combining electrical and photothermal performance.

Received 10th May 2025,
Accepted 5th June 2025

DOI: 10.1039/d5lp00136f

rsc.li/rscapplpolym

Introduction

Conjugated polymers, due to their unique π-conjugated backbones, can achieve efficient light absorption, charge transport, and structural tunability through molecular design, making them a promising material class for optoelectronic and energy-related applications.[1–4] The ability to tailor polymer backbones and side chains enables precise control over electronic and optical properties, making these materials increasingly attractive for applications in organic light-emitting diodes, organic photovoltaics, and organic field-effect transistors (OFETs).[1–8] In OFETs, molecular design and chain architecture are critical factors determining carrier mobility and overall device performance. Recent advancements include the incorporation of electron-deficient units and the optimization of side-chain structures, which have significantly improved n-type and ambipolar charge transport behaviors.[9–12] These improvements are important for achieving flexible, low-cost, and printable electronic devices, highlighting the growing potential of conjugated polymers in next-generation circuit architectures. Beyond traditional electronic applications, the multifunctionality of conjugated polymers enables their use in solar steam generation (SSG) systems, where materials capable of converting solar radiation into thermal energy are indispensable.[13–17]

Despite significant progress, n-type and ambipolar conjugated polymers still face critical challenges that limit their broader applications in electronic devices. One primary limitation is their poor environmental stability. Under environmental conditions, oxygen and moisture capture electrons, reducing charge transport performance.[18,19] Additionally, developing polymers with deep lowest unoccupied molecular orbital (LUMO) energy levels remains inherently challenging. While deep LUMO levels are crucial for efficient electron injection and enhanced air stability, achieving these levels without sacrificing charge mobility remains a significant design challenge.[20,21] To address these issues, recent studies have

[a]*Department of Materials Science and Engineering, Institute of Science Tokyo, Tokyo 152-8552, Japan. E-mail: michinobu.t.aa@m.titech.ac.jp*
[b]*Department of Chemical Engineering, National Taiwan University, Taipei 106, Taiwan. E-mail: cchueh@ntu.edu.tw*
[c]*Advanced Research Center for Green Materials Science and Technology, National Taiwan University, Taipei 10617, Taiwan*

†Electronic supplementary information (ESI) available. See DOI: https://doi.org/10.1039/d5lp00136f

‡These authors equally contributed to this work.

introduced a dual-acceptor strategy, incorporating two distinct electron-withdrawing units into the polymer backbone.[22–25] This approach not only enables more extended LUMO modulation but also enhances intramolecular charge delocalization, thereby improving electron transport efficiency.[26] Concurrently, the introduction of vinylene bridge units has emerged as a powerful method for reinforcing the planarity of the backbone. Vinylene linkers can act as structural locks, reducing torsional disorder and enhancing π–π orbital overlap, which promotes long-range charge delocalization. Both of these factors are critical for achieving high mobilities.[27]

For example, introducing a vinylene bridge into naphthalenediimide (NDI)-based dual-acceptor copolymers improves backbone planarity, reduces torsional disorder, and promotes π–π stacking.[28] As a result, electron mobilities significantly increase, effectively overcoming the limitations associated with environmental instability and shallow LUMO levels in conventional n-type systems.[29] Although these findings preliminarily reveal the importance of structural design in OFET applications, the broader multifunctional potential of vinylene-bridged conjugated polymers remains largely unexplored. In particular, the impact of vinylene-induced backbone rigidity on photothermal conversion remains to be evaluated. Given that effective photothermal materials require strong light absorption, efficient charge delocalization, and molecular-level heat dissipation, the extended conjugation of OFETs may also enhance the SSG performance.[30]

This study synthesized four vinylene-bridged naphthalenediimide (**vNDI**)-based conjugated polymers, each containing different second acceptor units with distinct rigidity and electron-withdrawing strengths. The incorporated units include benzothiadiazole (**S**), benzotriazole (**N**), triazolobenzothiadiazole (**NS**), and benzobistriazole (**NN**).[31] The structures of the target polymers are shown in Fig. 1. **vNDI-NS** and **vNDI-NN** exhibited more quinonoidal structures and stronger acceptor characteristics compared to **vNDI-S** and **vNDI-N**. As a result, **vNDI-NS** and **vNDI-NN** demonstrate broader light absorption and are expected to exhibit higher photothermal conversion efficiencies. Furthermore, conventional thiophene spacers have been replaced with selenophene spacers to enhance intermolecular interactions through the larger atomic size of selenium. Selenium has a stronger electron affinity than its corresponding thiophene unit, enhancing the electron transport properties of the polymer backbone.[32] Also, the conventional branched alkyl side chains have been replaced with silane side chains, improving chain stacking and solubility. These **vNDI**-based polymers showed considerable potential as active semiconducting layers in OFETs. The presence of electron-deficient **vNDI** cores and strong acceptor moieties promotes efficient n-type charge transport, while tailored backbone planarity and side-chain engineering facilitate precise regulation of molecular stacking and film morphology. Among them, **vNDI-N** and **vNDI-NS** exhibited more ordered molecular stacking as revealed by GIWAXS analysis, which is generally beneficial for charge transport in transistor structures. Conversely, the introduction of long and bulky alkyl chains into **vNDI-NN** and sulfur-induced steric distortion in **vNDI-S** disrupted regular π–π stacking, potentially reducing carrier mobility. Finally, we also evaluated the photothermal properties of the **vNDI**-based polymers and their applications in SSGs. The polymers were introduced into filter paper to fabricate SSG devices.

Experimental section

Materials

Tributyl(selenophen-2-yl)stannane, 1,1,1,2,2,2-hexabutyldistannane, (*E*)-1,2-bis(tributylstannyl)ethene, *N*-bromosuccinimide, tetrakis(triphenylphosphine)palladium(0), and common solvents such as tetrahydrofuran (THF), toluene, ethanol, dichloromethane (DCM), ethyl acetate (EA), hexane, methanol, acetone, chloroform (CF),

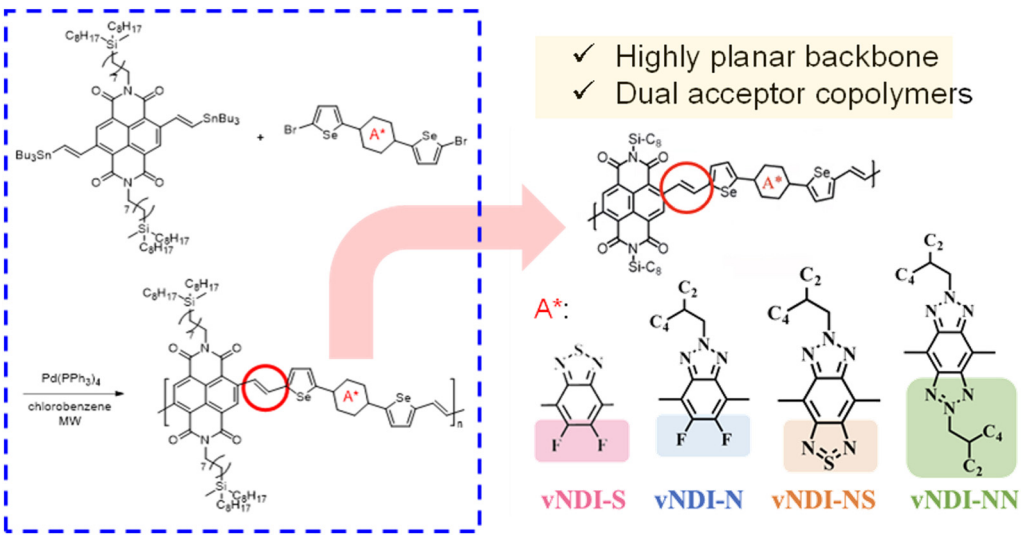

Fig. 1 Synthesis and design principles of **vNDI**-based polymers in this study.

and chlorobenzene (CB) for synthesis were purchased from Sigma-Aldrich. 4,7-Dibromo-5,6-difluoro-2,1,3-benzothiadiazole and 4,7-dibromo-2-(2-ethylhexyl)-5,6-difluoro-2*H*-benzotriazole were purchased from Luminescence Technology Corp. All chemicals were used as received without further purification.

Syntheses of monomers

4,9-Dibromo-2,7-bis(8-(methyldioctylsilyl)octyl)-naphthalenediimide, 2,7-bis(8-(methyldioctylsilyl)octyl)-4,9-bis((*E*)-2-(tributylstannyl)vinyl)naphthalenediimide (**vNDI**), 7-bis(5-bromoselenophen-2-yl)-5,6-difluorobenzothiadiazole (**S**), 4,7-bis(5-bromoselenophen-2-yl)-2-(2-ethylhexyl)-5,6-difluorobenzotriazole (**N**), 4,8-bis(5-bromoselenophen-2-yl)-6-(2-ethylhexyl)-[1,2,5]thiadiazolo[3,4-*f*]benzotriazole (**NS**), and 4,8-bis(5-bromoselenophen-2-yl)-2,6-bis(2-ethylhexyl)-1,6-dihydrobenzo[1,2-*d*:4,5-*d*′]bistriazolium (**NN**) were synthesized according to the methods reported in the literature.[28,32] For detailed information and characterization (Fig. S1–S5†), please refer to the ESI.†

Synthesis of NDI-based dual-acceptor polymers

The monomers **v-NDI** and **S/N/NS/NN**, along with the catalyst $Pd(PPh_3)_4$ (5 mol% relative to **v-NDI**), were added to a microwave vessel containing CB (0.1 M). The vessel was then sealed in a nitrogen-filled glovebox and subjected to microwave heating at 160 °C for 90 minutes under Stille coupling conditions. At the same temperature, 2-(tributylstannyl)thiophene and 2-bromothiophene (each at 1.1 equivalents relative to **v-NDI**) were sequentially added, and the reaction was carried out for 15 minutes to perform the end-capping reaction. After cooling to room temperature, the reaction mixture was poured into methanol, and the precipitate was filtered and collected. Soxhlet extraction was performed using various solvents. Acetone and hexane were used to remove residual catalysts and oligomers, while the desired product was extracted with CF. The CF solution was concentrated under vacuum and slowly added to methanol to obtain the target polymers. Finally, the polymers were collected by filtration and dried under vacuum. For detailed information and characterization (Fig. S6–S9†), please refer to the ESI.†

OFET fabrication and characterization

Bottom-gate/top-contact (BG/TC) transistor devices were fabricated in this work. Highly n-doped silicon wafers (100) were used as substrates with a 300 nm SiO_2 dielectric layer (areal capacitance = 10 nF cm^{-2}). Prior to device fabrication, the wafers were exposed to UV/ozone for 1 hour. A self-assembled monolayer of *n*-octadecyltrichlorosilane (ODTS) was subsequently deposited onto the dielectric layer by spin-coating its precursor solution (15 μL of ODTS in 15 mL of trichloroethylene) at 3000 rpm for 10 seconds in a glovebox. Note that the chemical reaction between ODTS and SiO_2 is accelerated by the presence of NH_3 gas and continues overnight. The sample was then ultrasonicated in toluene for 15 minutes to remove residual chemicals. Prior to depositing the active layer, the ODTS-modified wafers were partially covered with polydimethylsiloxane (PDMS) and subjected to 8 minutes of plasma treatment to form a hydrophilic boundary. Polymer solutions of **vNDI-N**, **vNDI-S**, **vNDI-NS**, or **vNDI-NN** were prepared in CF (5 mg mL^{-1}) and stirred for 4.5 hours in a glovebox. Before spin-coating, the polymer solution was filtered through a 0.22 μm filter. Then, spin-coating was performed at 2000 rpm for 60 seconds in a glovebox, followed by annealing at a specific temperature (150 °C, 200 °C, or 250 °C) and an optimized time (10 or 30 minutes) to prepare the film. Finally, top-contact gold electrodes were deposited *via* thermal evaporation using a shadow mask, with channel length (L) of 50 μm and channel width (W) of 1000 μm. The performance of the OFETs was characterized using a Keithley 4200-SCS semiconductor parameter analyzer (Keithley Instruments Inc.) in a glovebox.

SSG device fabrication and characterization

This study investigated the photothermal and SSG properties of **vNDI**-based polymers using a membrane-based system. Commercial filter paper (Kiriyama, No. 5B; particle retention: 4 μm; thickness: 0.22 mm) was selected as the substrate. Due to the randomly arranged cellulose fiber networks of the filter paper, it provides an ideal structural scaffold for photothermal membranes in SSG applications.[33] The inherent porous structure facilitates water uptake and capillary transport. The **vNDI**-based polymers were dissolved in CF (5 mg mL^{-1}) by heating and stirring at 50 °C for 4 hours, then deposited onto the filter paper using a micropipette in a dropwise manner (10 μL × 10 times). The resulting membranes were dried under vacuum at room temperature overnight. This preparation method ensures uniform adsorption and fixation of the polymer layer on one side of the filter paper substrate. The surface morphology of the resulting photothermal membranes was examined using optical microscopy (OM) (Fig. S10†), and static water contact angle measurements were performed on the top surface (inset of Fig. S10†) to evaluate the wetting characteristics.

Results and discussion

Synthesis and characterization of polymers

The target polymers were synthesized *via* the Stille polycondensation method (Fig. 1), and their chemical structures were confirmed by ^{1}H NMR (Fig. S6–S9†). The number-average molecular weights (M_n) of **vNDI-S**, **vNDI-N**, **vNDI-NS**, and **vNDI-NN** were 33, 47, 7, and 8 kDa, respectively, and the corresponding polydispersity indices (M_w/M_n) estimated by GPC were 2.7, 2.3, 1.2, and 1.8, respectively. When testing their molecular weights, we found that **vNDI-NS** and **vNDI-NN** did not fully dissolve in CF. We believe this is the primary cause of their lower molecular weights. All four polymers exhibited good thermal stability, with a 5% weight loss temperature ($T_d^{5\%}$) greater than 387 °C, as shown in Fig. 2a and Table 1. Note that **vNDI-N** contains a 1,2,3-triazole (N–N–N) structure with a branched alkyl chain on the central nitrogen, which shows superior thermal stability compared to **vNDI-S**. This is because the triazole structure provides better resonance stabilization, stronger bonding

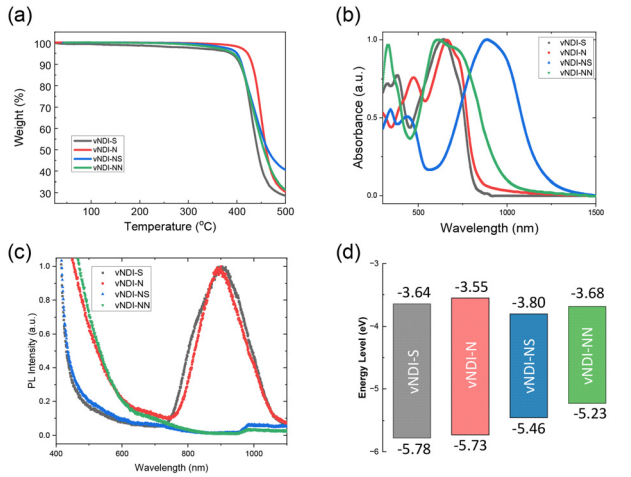

Fig. 2 (a) TGA thermograms, (b) UV-vis-NIR film absorption spectra, (c) photoluminescence (PL) emission spectra, and (d) energy levels (obtained) by cyclic voltammetry (CV) of **vNDI**-based polymer films.

Table 1 Thermal, optical, and electrochemical properties of **vNDI**-based polymers

vNDI-	$\lambda_{max,\ film}$ [a] (nm)	E_g^{opt} [b] (eV)	HOMO[c] (eV)	LUMO[c] (eV)	$T_d^{5\%}$ [d] (°C)
S	643	1.56	−5.78	−3.64	387
N	662	1.50	−5.73	−3.55	422
NS	888	1.05	−5.46	−3.80	400
NN	615	1.30	−5.23	−3.68	392

[a] Thin-film absorption maximum. [b] Optical bandgap estimated from the absorption onset of polymer films. [c] Estimated from the onset oxidation/reduction potentials. [d] 5% weight loss temperature.

interactions, and the possibility of non-covalent contacts (*e.g.*, N···Se), while the side chains offer steric protection.[34,35] Notably, **vNDI-NS** maintained high thermal stability ($T_d^{5\%}$ = 400 °C) despite containing the same N–S–N moiety as **vNDI-S**. This is attributed to the stabilizing effect of the opposing N–N–N ring.[36,37] Asymmetric substitution promotes favorable molecular stacking, where the triazole unit compensates for the weaker thiadiazole unit, maintaining overall thermal robustness.

Optical properties

Fig. 2b shows the ultraviolet-visible-near-infrared (UV–vis–NIR) absorption spectra of these polymers in the thin-film states, and Table 1 summarizes the main spectral data. All polymers displayed absorption characteristics in the UV-vis region. **vNDI-NS** exhibited the most red-shifted intramolecular charge-transfer (ICT) absorption, extending beyond 1100 nm, indicating the strongest electron donor–acceptor interaction and the narrowest bandgap (E_g).[38] **vNDI-NN** showed strong absorption around 850 nm, with distinct vibronic features in the π–π* region, suggesting enhanced backbone planarity and aggregation.[39] In contrast, **vNDI-N** displayed a slightly blue-shifted ICT peak with moderate aggregation-induced characteristics. **vNDI-S** exhibited the weakest and most blue-shifted ICT band, with minimal spectral changes in the solid state, indicating limited intermolecular interactions and a larger E_g.

The photoluminescence (PL) spectra of these films were also measured as shown in Fig. 2c. When illuminated with incident light at 385 nm, the **vNDI-S** and **vNDI-N** films exhibited PL at 904 and 900 nm, respectively. On the other hand, **vNDI-NS** and **vNDI-NN** showed no luminescence. The fluorescence quantum yields (Φ_f) and lifetimes (τ) of **vNDI-S** and **vNDI-N** were measured, as summarized in Table S1.† Based on Φ_f and τ, the radiative decay rate constant (k_r) and non-radiative decay rate constant (k_{nr}) were estimated using the following equations:

$$\Phi_f = \frac{k_r}{k_r + k_{nr}} \quad (1)$$

$$\tau = \frac{1}{k_r + k_{nr}} \quad (2)$$

The results suggest that **vNDI-S** and **vNDI-N** exhibited similar optical properties in both absorption and PL spectra. Therefore, their k_r and k_{nr} values were also similar, with $k_r \sim 10^6\ s^{-1}$ and $k_{nr} \sim 10^8\ s^{-1}$.

Electrochemical properties

The electrochemical properties of these polymers were evaluated using cyclic voltammetry (CV), with the results summarized in Table 1. The highest occupied molecular orbital (HOMO) energy levels and the LUMO energy levels were estimated from the onset oxidation and reduction potentials, respectively (Fig. S11†). The HOMO and LUMO energy levels and E_gs of these four polymers are significantly influenced by the second acceptor units. **vNDI-S** and **vNDI-N** displayed deeper HOMO energy levels and shallower LUMO energy levels. This result indicates that the triple-fused heterocyclic compounds have significantly narrowed E_gs. Compared to **vNDI-N** containing difluorobenzotriazole (HOMO: −5.73 eV, LUMO: −3.55 eV), **vNDI-S** containing a second acceptor of difluorobenzothiadiazole exhibited slightly deeper HOMO (−5.78 eV) and LUMO (−3.64 eV) energy levels. The same applies to **vNDI-NS** (HOMO: −5.46 eV, LUMO: −3.80 eV) and **vNDI-NN** (HOMO: −5.23 eV, LUMO: −3.68 eV). This result indicates that the benzotriazole unit is a stronger donor than the benzothiadiazole unit. In other words, the benzothiadiazole unit is a stronger acceptor than the benzotriazole unit. The electrochemical E_gs are related to the optical E_gs because electron transfer and electronic transitions involve the same orbitals.[40,41]

Molecular simulations

To investigate the electronic structures of **vNDI**-based polymers, we performed density functional theory (DFT) calculations. All calculations were carried out using the B3LYP functional and 6-31G(d) basis set, implemented in the Gaussian 16 software package. To reduce computational complexity, we

adopted trimer models with simplified alkyl side chains (substituted by methyl groups). Fig. 3 shows the frontier molecular orbitals (FMOs) of trimers, and Table S2† summarizes the corresponding energy levels. The overall trend of HOMO and LUMO energy levels is consistent with the experimental results, but the experimentally determined E_gs are larger than those calculated by DFT. This is a common result because DFT does not account for quasiparticle corrections (*e.g.*, GW) or include recombination energy and charge transfer shielding effects.[40,42]

FMO analysis indicated that the HOMOs of all four **vNDI**-based polymers are delocalized along the polymer backbone. In contrast, the distribution of LUMOs varies depending on the structural motif. For **vNDI-S** and **vNDI-N**, LUMOs are predominantly localized on the NDI core. In the case of **vNDI-NN**, although the NDI segment remained the primary localization site, the LUMO extended throughout the benzobistriazole unit. For **vNDI-NS**, the LUMO was more uniformly distributed along the backbone. These results suggest that introducing stronger electron-accepting units modulates electron distribution, particularly affecting LUMO characteristics, and provides an effective strategy for adjusting polymer energy levels. This redistribution of orbital density is consistent with the bathochromic shifts observed in the absorption spectrum.

Morphological characterization

We utilized atomic force microscopy (AFM) and grazing-incidence wide-angle X-ray scattering (GIWAXS) measurements to investigate the influence of structural differences on the morphology and crystalline properties of these polymer films. The samples were prepared by spin-coating polymer solutions onto Si substrates with a 300 nm-thick SiO_2 dielectric layer, followed by annealing at different temperatures and times (**vNDI-S** at 200 °C for 30 minutes; **vNDI-N**, **vNDI-NN**, and **v-NDI-NS** at 250 °C for 10 minutes). As shown in Fig. 4a–d, all films exhibited smooth surface morphologies with low root-mean-square (RMS) values. Interestingly, among the four samples, the triple-fused ring polymers, **vNDI-NS** and **vNDI-NN**, displayed the highest and smallest RMS values (809.4 pm and 420.3 pm, respectively). This result indicates that the triple-fused ring polymers exhibit unique film morphologies. For **vNDI-NS**, the relatively high RMS value can be attributed to the strong self-assembly properties of the **NS** units. The formation of cluster-like crystalline domains leads to a rough surface. On the other hand, the symmetrical triple-fused structure of **vNDI-NN** may facilitate moderate molecular stacking, resulting in a smooth morphology. **vNDI-N** and **vNDI-S** exhibited moderate roughness values, indicating that the **vNDI** moiety is the primary driving force for aggregation, while the second acceptor units have a relatively minor influence on morphology.

GIWAXS was used to evaluate the crystallinity and chain stacking behavior of films. The 2D GIWAXS patterns are shown in Fig. S12,† while the 1D line-cut profiles extracted from the 2D patterns are shown in Fig. 4e–h. The 1D line-cut profiles clearly exhibited two distinct trends: one group containing **vNDI-N** and **vNDI-NS**, and the other group containing **vNDI-S** and **vNDI-NN**. The 1D profile of **vNDI-N** showed prominent out-of-plane (100) and (200) scattering peaks, indicating an edge-on orientation and more ordered lamellar stacking. Similarly, the 1D profile of **vNDI-NS** showed a trend like that of **vNDI-N**. Table S3† shows the crystalline coherent length (CCL) and *d*-spacing (DS) calculated based on the scattering peaks in the 1D line-cut profiles. The results showed that although **vNDI-NS** exhibited a similar trend, its CCL value (97.58 Å) is lower than that of **vNDI-N** (165.15 Å). This difference may be attributed to the interference of the S substituent. **vNDI-N** exhibited intramolecular Se–F interactions, whereas **vNDI-NS** lacked this conformational locking effect due to the additional benzothiadiazole annulation, resulting in decreased crystallinity. In contrast, the other groups, **vNDI-S** and **vNDI-NN**, exhibited a higher proportion of amorphous structures (Fig. 4e, h and Fig. S12c, d†). Based on these results, we propose that the introduction of the S substituent disrupts the overall structural consistency and leads to disordered molecular stacking. Notably, despite the N-dominated structure of **vNDI-NN**, its crystallinity remains poor, which may be attributed to the absence of intramolecular conformational locking and the excessive flexibility of the long alkyl chains, leading to a disordered arrangement.

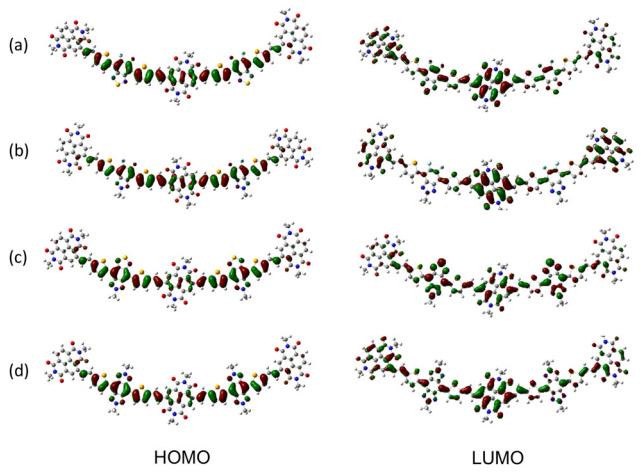

Fig. 3 Frontier molecular orbitals (FMOs) of trimer backbones calculated using DFT based on (a) **vNDI-S**, (b) **vNDI-N**, (c) **vNDI-NS**, and (d) **vNDI-NN**.

Characterization of OFET devices

The charge transport properties of these four polymers were evaluated by fabricating bottom-gate/top-contact (BGTC) OFETs. Detailed information on device fabrication and characterization is described in the ESI.† Fig. 5a shows the best transfer curves of OFETs based on these polymer films under different annealing conditions (**vNDI-S** at 200 °C for 30 minutes; **vNDI-N**, **vNDI-NN**, and **v-NDI-NS** at 250 °C for 10 minutes). Fig. 5b presents the corresponding hole and electron mobilities, and Table S4† summarizes the detailed transistor performance. Although all polymers displayed ambipolar charge transport behavior, the mobilities of **vNDI-NS** and

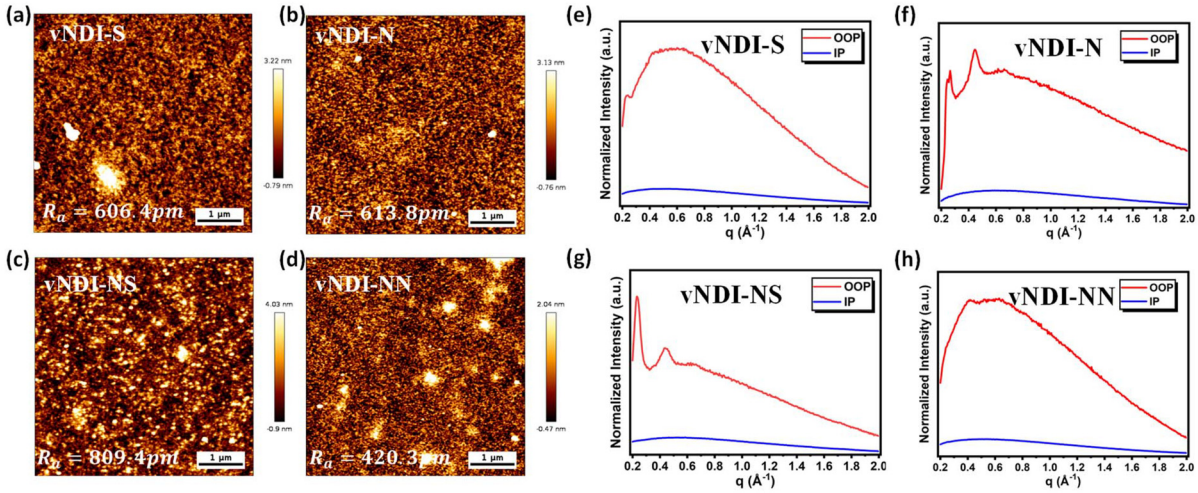

Fig. 4 (a–d) AFM images and (e–h) 1D line-cut profiles extracted from 2D GIWAXS patterns of **vNDI**-based polymer thin films.

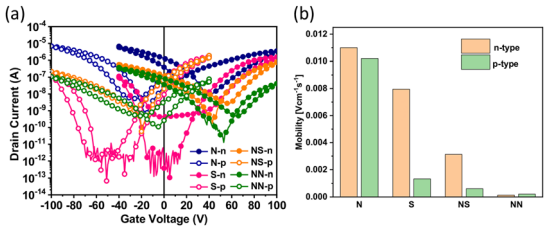

Fig. 5 (a) Transfer curves and (b) mobilities of the optimized FET devices based on **vNDI**-based polymers.

vNDI-NN were lower than those of **vNDI-S** and **vNDI-N**. This can be attributed to the molecular weight issues. As reported in many studies, molecular weight is closely related to the carrier mobility, and a positive relationship can be observed before molecular weight saturation.[43] Therefore, the low molecular weights of **vNDI-NS** and **vNDI-NN** may be the primary cause of their poor mobilities. Regarding **vNDI-N** and **vNDI-S**, **vNDI-N** exhibited higher charge transport properties, which was attributed to its higher crystallinity. Although the electron mobility of **vNDI-S** was similar to that of **vNDI-N**, its hole mobility decreased significantly, which was due to its deeper HOMO energy level, resulting in a larger hole injection barrier and poorer hole transport properties.

Photothermal properties

Given the unique absorption characteristics of these four polymers, we next investigated and compared their performance in photothermal and solar steam generation (SSG) applications. To conduct this study, we coated the polymers onto commercial filter paper to prepare photothermal membranes. The surface morphology of the photothermal membranes was examined using an optical microscope, as shown in Fig. S10.† The water contact angle measurements revealed that the surface exhibited a Janus structure, with the upper surface being hydrophobic (θ value: 105–120°) and the lower surface being hydrophilic (Fig. S10†).[44] An infrared thermal imaging camera was used to monitor surface temperature changes under simulated solar irradiation. After continuous irradiation for 6 minutes, thermal images of the dry membranes were recorded. The surface temperature of untreated filter paper (without polymer coating) was 33.3 °C. In contrast, the surface temperature of the filter membranes coated with **vNDI**-based polymers was higher, indicating effective photothermal conversion. Specifically, the surface temperatures of the filter membranes containing **vNDI-S**, **vNDI-N**, **vNDI-NS**, and **vNDI-NN** were 55.2 °C, 57.8 °C, 68.1 °C, and 65.9 °C, respectively. These trends are consistent with the absorption and PL characteristics of the corresponding polymers. The photothermal response profiles under simulated sunlight showed a rapid temperature increase within the first minute of irradiation (Fig. 6a). To assess photothermal stability and reversibility, the membranes were subjected to four irradiation cycles, each consisting of 2 minutes of light exposure followed by 2 minutes of rest, as displayed in Fig. 6b. Consistent final temperatures were obtained after each irradiation cycle, confirming the excellent photostability and reusability of the photothermal membranes under repeated operating conditions.

To evaluate the performance of SSG, the membranes coated with **vNDI**-based polymers were placed over the mouth of a plastic bottle filled with deionized water, ensuring that only the photothermal membranes were directly exposed to simulated sunlight. The entire setup was placed on an electronic balance to monitor water mass loss in real time during irradiation, providing a quantitative assessment of SSG efficiency. Under simulated solar irradiation, the surface temperatures of the photothermal membranes and the corresponding mass losses were recorded over a 20-minute period, as shown in Fig. 6c and d. The solar-to-vapor conversion efficiency (η) was determined as the ratio of the energy required for water evaporation to the total incident light

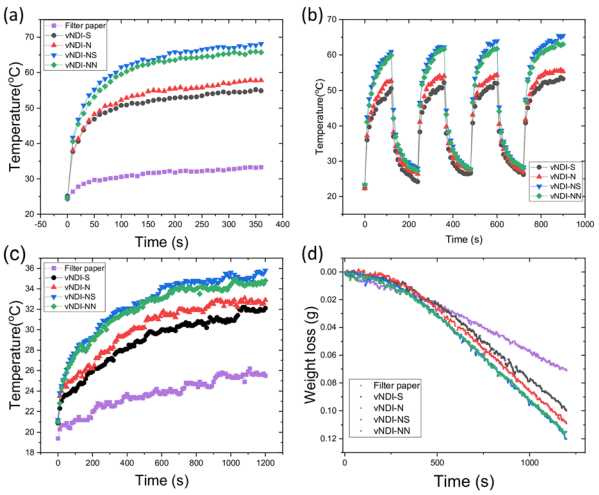

Fig. 6 Temperature changes in (a) dry and (c) wet photothermal membranes with **vNDI**-based polymers and filter paper (control sample) under simulated sunlight irradiation for 6 minutes. (b) The repeated simulated sunlight irradiation at intervals of 2 minutes. (d) The weight loss of wet photothermal membranes with **vNDI**-based polymers under simulated sunlight irradiation for 20 minutes.

energy. A calibrated solar simulator (AM 1.5G) was used to maintain light intensity at 1000 W m^{-2}, and a standard silicon reference cell was used for calibration. To ensure accuracy, the baseline water evaporation rate under dark conditions was measured separately and subtracted from the irradiation values. The η values of the membranes containing **vNDI-S**, **vNDI-N**, **vNDI-NS**, and **vNDI-NN** were 47.4%, 52.3%, 58.3%, and 56.4%, respectively. In contrast, the efficiency of the control sample (uncoated filter paper) was 31.2%. These results are consistent with the temperature profiles observed for each photothermal membrane, further highlighting the correlation between photothermal conversion and evaporation efficiency.

Conclusions

In this study, we designed and synthesized a series of vinylene-bridged naphthalenediimide (**vNDI**)-based copolymers with a dual-acceptor architecture to investigate their multifunctional performance in OFET and SSG devices. By incorporating structurally diverse second acceptors, selenium-based spacers, and silane side chains, these polymers exhibited tunable energy levels, enhanced backbone planarity, and optimized molecular stacking. Among the series, **vNDI-N** demonstrated the highest ambipolar charge mobilities in OFETs, attributed to its improved crystallinity and favorable π–π stacking. Note that the lower molecular weights of **vNDI-NS** and **vNDI-NN** may have limited the crystallinity and electron transport properties. However, in SSG applications, the **vNDI-NS**-based photothermal membrane achieved the highest solar-to-vapor conversion efficiency due to its narrow bandgap and strong intramolecular charge transfer. These findings highlight the effectiveness of molecular design in regulating the optoelectronic and photothermal properties of dual-acceptor-type conjugated copolymers.

Data availability

The data that support the findings of this study are available from the corresponding authors upon reasonable request.

Conflicts of interest

There are no conflicts to declare.

Acknowledgements

This study was partly supported by JSPS KAKENHI Grant Number JP24H00005 (T. M.). C.-Y. L. thanks the Japan-Taiwan Exchange Association for a scholarship. W. H. thanks Grant-in-Aid for JSPS Fellows (23KF0223). C.-C.C. is thankful for the financial support from the National Science and Technology Council (NSTC) in Taiwan (112-2223-E-002-008-MY4, 113-2628-E-002-015-MY3, and 113-2124-M-027-001) and the Top University Project of National Taiwan University (114L7745, 114L895203, and 114L104305). We thank the Core Facility Center, Institute of Science Tokyo, for GPC measurements.

References

1 X. Zhao and X. Zhan, *Chem. Soc. Rev.*, 2011, **40**, 3728–3743.
2 B. Kuei and E. D. Gomez, *Soft Matter*, 2017, **13**, 49–67.
3 Y. Wang, S. Sun, Y. Huang, Y. Fu, J. Qi, K. Tie, Z. Wang, F. Jiao, R. Si, X. Chen, L. Li and W. Hu, *Aggregate*, 2023, **4**, e379.
4 X. Cao and Y. Han, *Aggregate*, 2024, **5**, e501.
5 S. Xu, Y. Liu and S. Cao, *Macromol. Symp.*, 2008, **270**, 161–170.
6 J. Kimpel and T. Michinobu, *Polym. Int.*, 2021, **70**, 367–373.
7 G. Zhang, F. R. Lin, F. Qi, T. Heumüller, A. Distler, H.-J. Egelhaaf, N. Li, P. C. Y. Chow, C. J. Brabec, A. K.-Y. Jen and H.-L. Yip, *Chem. Rev.*, 2022, **122**, 14180–14274.
8 L. Wang, Z. Yi, Y. Zhao, Y. Liu and S. Wang, *Chem. Soc. Rev.*, 2023, **52**, 795–835.
9 Y. Ji, C. Xiao, G. H. Heintges, Y. Wu, R. A. Janssen, D. Zhang, W. Hu, Z. Wang and W. Li, *J. Polym. Sci., Part A: Polym. Chem.*, 2016, **54**, 34–38.
10 L. Ding, Z.-D. Yu, X.-Y. Wang, Z.-F. Yao, Y. Lu, C.-Y. Yang, J.-Y. Wang and J. Pei, *Chem. Rev.*, 2023, **123**, 7421–7497.
11 D. Liu, Y. Zhao, J. Zhang, Z. Wei, Y. Liu and Y. Wang, *Angew. Chem., Int. Ed.*, 2024, **63**, e202400061.
12 S. Ma, H. Li, W. Wu, S. Gámez-Valenzuela, R. Ma, Q. Bai, J. Zhong, S. Y. Jeong, Q. Liu, H. Zhang, G. Zhang, W. Zhang, J. Chen, E. Huang, B. Liu, K. Feng, H. Y. Woo, L. Niu, H. Sun and X. Guo, *Angew. Chem., Int. Ed.*, 2025, **64**, e202423616.

13 C.-Y. Lin and T. Michinobu, *Beilstein J. Nanotechnol.*, 2023, **14**, 454–466.
14 S. V. Kamath, K. Aruchamy and N. S. Kotrappanavar, in *Polymer-Based Advanced Functional Composites for Optoelectronic and Energy Applications*, Elsevier, 2021, pp. 31–49.
15 J. W. Lim, *Materials*, 2024, **17**, 3698.
16 S. Wageh, W. Boukhili and A. Al-Ghamdi, *Phys. Status Solidi A*, 2022, **219**, 2100500.
17 C. Xu, R. Ye, H. Shen, J. W. Y. Lam, Z. Zhao and B. Z. Tang, *Angew. Chem., Int. Ed.*, 2022, **61**, e202204604.
18 M. Nakano, I. Osaka and K. Takimiya, *Macromolecules*, 2015, **48**, 576–584.
19 K. Takimiya and M. Nakano, *Bull. Chem. Soc. Jpn.*, 2018, **91**, 121–140.
20 L. Zhao, W. Li, H. Qin, X. Yi, W. Zeng, Y. Zhao and H. Chen, *Macromolecules*, 2023, **56**, 2990–3003.
21 H. Chen, R. Xie, J. Tang, X. Liu, J. Li, C. Liu, Y. Qiang, C. Yang, L. Zhang and J. Chen, *Macromolecules*, 2025, **58**, 1011–1022.
22 Q. Liu, Y. Wang, Y. Ren, A. Kohara, H. Matsumoto, Y. Chen, S. Manzhos, K. Feron, S. E. Bottle, J. Bell, Y. Zhou, T. Michinobu and P. Sonar, *ACS Appl. Electron. Mater.*, 2020, **2**, 1609–1618.
23 Q. Liu, W. He, Y. Shi, S. Otep, W. L. Tan, S. Manzhos, C. R. McNeill, X. Guo, P. Sonar, T. Michinobu and A. K. K. Kyaw, *Chem. Mater.*, 2022, **34**, 3140–3151.
24 W.-C. Lin, J. Jayakumar, C.-L. Chang, L.-Y. Ting, T.-F. Huang, M. H. Elsayed, A. M. Elewa, Y.-T. Lin, J.-J. Liu, Y.-T. Tseng and H.-H. Chou, *J. Mater. Chem. A*, 2022, **10**, 6641–6648.
25 D. Patra, X. Zhan, R. Linthoinganbi, S. Muduli, S. Mishra, Y. Liu and S. Park, *J. Mater. Chem. C*, 2023, **11**, 1457–1463.
26 Z. Jiang, D. Liu, Y. Wang, W. Song, D. Yan, Z. Ge and Y. Liu, *Angew. Chem., Int. Ed.*, 2025, **64**, e202416669.
27 Y. Wang, T. Hasegawa, H. Matsumoto and T. Michinobu, *J. Am. Chem. Soc.*, 2019, **141**, 3566–3575.
28 Y.-S. Wu, C.-Y. Tsai, D. D. Thanh, Y.-H. Shih, H.-T. Cheng, T. Michinobu, W.-C. Chen and C.-C. Chueh, *ACS Appl. Polym. Mater.*, 2024, **6**, 5900–5909.
29 Y. Wang, H. Wang, J. Deng, Y. Pan, Z. Zheng and X. Ding, *Macromol. Rapid Commun.*, 2023, **44**, 2300244.
30 I. M. Mekhemer, Y. S. Wu, A. M. Elewa, W. C. Chen, C. C. Chueh and H. H. Chou, *Sol. RRL*, 2024, **8**, 2300994.
31 Y. Wang and T. Michinobu, *J. Mater. Chem. C*, 2016, **4**, 6200–6214.
32 R. Acharya, S. Cekli, C. J. Zeman IV, R. M. Altamimi and K. S. Schanze, *J. Phys. Chem. Lett.*, 2016, **7**, 693–697.
33 C. Y. Lin, S. Shimizu, Y. Sagara, H. Matsumoto and T. Michinobu, *Sol. RRL*, 2025, **9**, 2400803.
34 Z. Liu, G. Zhang and D. Zhang, *Acc. Chem. Res.*, 2018, **51**, 1422–1432.
35 M. M. Alam, *Arch. Pharm.*, 2022, **355**, 2100158.
36 E. Jansson, P. C. Jha and H. Ågren, *Chem. Phys.*, 2006, **330**, 166–171.
37 A. Garzón, J. M. Granadino-Roldán, M. Moral, G. García, M. P. Fernández-Liencres, A. Navarro, T. Peña-Ruiz and M. Fernández-Gómez, *J. Chem. Phys.*, 2010, **132**, 064901.
38 D.-H. Lim, J.-W. Ha, H. Choi, S. C. Yoon, B. R. Lee and S.-J. Ko, *Nanoscale Adv.*, 2021, **3**, 4306–4320.
39 R. Noriega, J. Rivnay, K. Vandewal, F. P. Koch, N. Stingelin, P. Smith, M. F. Toney and A. Salleo, *Nat. Mater.*, 2013, **12**, 1038–1044.
40 H. Sun and J. Autschbach, *J. Chem. Theory Comput.*, 2014, **10**, 1035–1047.
41 J. Bertrandie, J. Han, C. S. De Castro, E. Yengel, J. Gorenflot, T. Anthopoulos, F. Laquai, A. Sharma and D. Baran, *Adv. Mater.*, 2022, **34**, 2202575.
42 C. S. Sarap, Y. Singh, J. M. Lane and N. Rai, *Sci. Rep.*, 2023, **13**, 21587.
43 D. K. Tran, A. Robitaille, I. J. Hai, C.-C. Lin, D. Kuzuhara, T. Koganezawa, Y.-C. Chiu, M. Leclerc and S. A. Jenekhe, *Chem. Mater.*, 2022, **34**, 9644–9655.
44 M. Wang, C.-Y. Lin, Y. Sagara and T. Michinobu, *ACS Mater. Au*, 2024, **4**, 82–91.